ACS APPLIED MATERIALS & INTERFACES

Research Article

www.acsami.org

2D $ZnIn_2S_4$ Nanosheet/1D TiO_2 Nanorod Heterostructure Arrays for Improved Photoelectrochemical Water Splitting

Qiong Liu,[†] Hao Lu,[†] Zhiwei Shi,[†] Fangli Wu,[†] Jun Guo,[‡] Kaimo Deng,[†] and Liang Li*[,†]

[†]College of Physics, Optoelectronics and Energy & Collaborative Innovation Center of Suzhou Nano Science and Technology, Soochow University, Suzhou 215006, P. R. China

[‡]Analysis and Testing Center, Soochow University, Suzhou, P. R. China

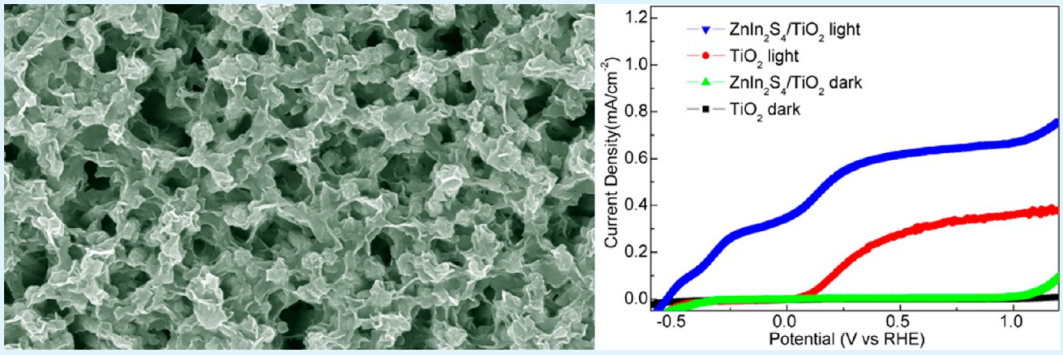

ABSTRACT: We report the fabrication of 2D $ZnIn_2S_4$ nanosheet/1D TiO_2 nanorod heterojunction arrays by a facile hydrothermal process and their use as photoelectrodes in a photoelectrochemical (PEC) cell for high-performance solar water splitting. The morphology, microstructure, and phase of pristine TiO_2 and 2D $ZnIn_2S_4$ nanosheet/1D TiO_2 nanorod heterojunction arrays were characterized in detail. PEC measurements showed that 2D/1D heterojunction arrays offered enhanced photocurrent density (3 times higher than that of pristine TiO_2), negatively shifted onset potential from 0.05 to −0.53 V, and high light on/off cycle stability. Electrochemical impedance investigation attested to a significant improvement of the interface electron transfer kinetics in this heterojunction, thus facilitating electron−hole separation, transfer, and collection, which resulted in enhanced PEC properties.

KEYWORDS: *photoelectrochemical cell, $ZnIn_2S_4$, TiO_2, nanosheets, nanorods, heterojunction*

1. INTRODUCTION

Solar water splitting to hydrogen and oxygen is one of the most promising forms of energy production, since both water and sunlight are abundant on earth. Fujishima and Honda first demonstrated a photoelectrochemical (PEC) approach to realize water splitting using TiO_2 electrodes in 1972.[1] Subsequently, a variety of photoactive materials have been investigated and optimized to improve PEC properties based on these considerations: small band-gap semiconductors with wide spectrum response, a proper conduction/valence band position satisfying water oxidization and reduction potentials, fast carrier separation and transportation, and stability, and so on.[2,3] Unfortunately, no single material can meet all of these requirements. Among metal oxide semiconductors, TiO_2 has been widely studied due to its high resistance to photocorrosion, low-cost, and abundance.[4−7] However, TiO_2 has a large band gap (3.0 eV), low electron mobility (1 $cm^2/V/s$), and short hole diffusion length (10−100 nm), which limit its quantum efficiency.[8,9] Various strategies have been investigated to attack these problems. In order to reduce the band gap, TiO_2 is doped with different heteroatoms, such as transition metals, nitrogen, and carbon.[10,11] One-dimensional (1D) nanostructures (nanorods and nanotubes) can provide a short diffusion length perpendicular to the charge collecting substrate, yielding a low recombination of electron−hole pairs.[12,13] Furthermore, hierarchical and branched nanostructures simultaneously provide the advantages of a rapid charge transfer pathway for carrier collection, a large surface area for increased reaction sites, and excellent light trapping.[14−17] Other effective routes, including plasmonic assistance, cocatalysis, and heterostructures, are also utilized.[18−20] Although many methods have been developed, the efficiency of a TiO_2-based PEC cell is still low, and further research is necessary, particularly designing new architectures for photoelectrodes.

As an important II-III_2-VI_4 semiconductor, ternary sulfide $ZnIn_2S_4$ with a 2D layer structure has attracted increasing attention due to its potential applications in different fields, such as thermoelectricity, photoconduction, charge storage, and so on.[21,22] Since Lei et al. first used $ZnIn_2S_4$ as a visible-light-driven photocatalyst for hydrogen production,[23] many reports have focused on synthesizing $ZnIn_2S_4$ nanomaterials with various morphologies and improving their PEC performance.[24−26]

Received: July 30, 2014
Accepted: September 16, 2014
Published: September 16, 2014

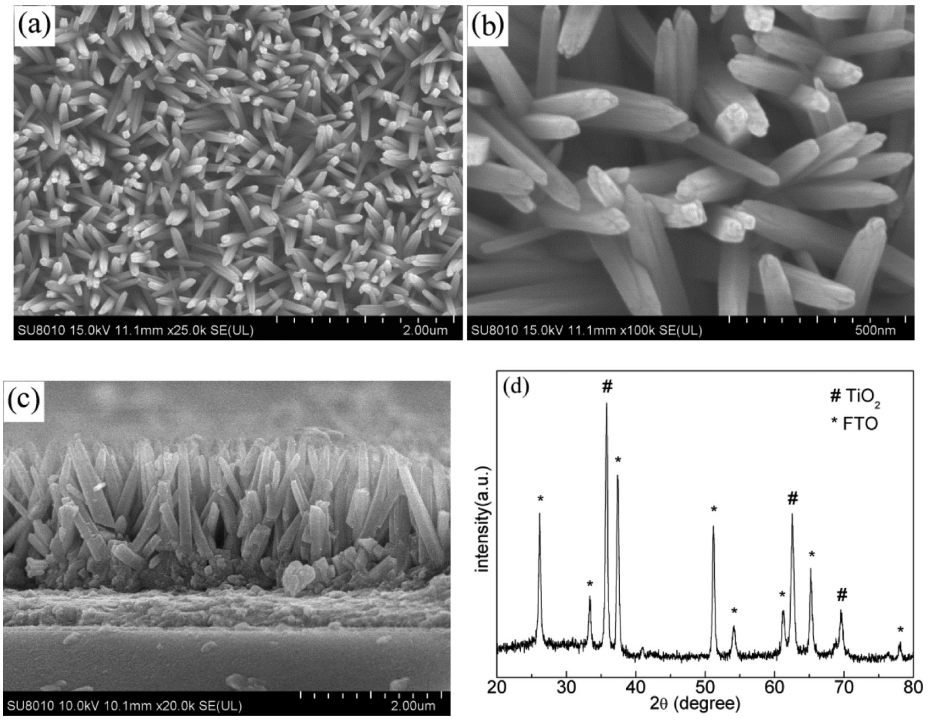

Figure 1. Representative SEM images of TiO_2 nanorod arrays grown on FTO substrates. (a, b) Top view. (c) Cross-sectional view. The corresponding XRD pattern is shown in (d).

Compared with 1D systems, 2D materials demonstrate unique characteristics for applications in photoelectrochemical cells, for example, the decoupling of the directions of light absorption and charge collection; the larger surface area promotes charge migration across both the semiconductor/electrolyte and the semiconductor/photoelectrode interface; increased photon−matter interaction via multiple reflection and scattering at the semiconductor/electrolyte interface, etc.[27] To fully integrate the above-mentioned advantages of the single units, the concept of 2D/1D nanoheterojunctions was proposed. Up to now, little effort has been paid to the growth of 2D nanosheets on 1D nanomaterials, which might arise from the difficult control of different growth models of 1D and 2D materials in one synthetic system.[28−31]

In the present work, we report the synthesis of 2D $ZnIn_2S_4$ nanosheet/1D TiO_2 nanorod heterojunction arrays by a facile hydrothermal process and their PEC properties. It was found that this hybrid structure could significantly promote the PEC properties of the TiO_2 photoelectrodes, including the photocurrent density and the onset potential. The electrochemical and PEC properties are investigated in detail to reveal the origin of the synergistic effect of the heterojunction.

2. EXPERIMENTAL SECTION

2.1. Synthesis of TiO_2 Nanorod Arrays. In a typical synthesis process, 2.84 mmol of citrate, 2.84 mmol of tetrabutyl titanate, and 30 mL of concentrated hydrochloric acid (36−38% by weight) were added into 30 mL of deionzied water. The mixture was stirred for 15 min and then transferred to a Teflon-lined stainless steel autoclave with a 20 mL capacity. The cleaned FTO substrate was placed into the solution with the conductive surface downward. Then, the autoclave was sealed and heated at 150 °C for 6 h. After cooling to room temperature, the growth substrate was taken out for rinsing with deionized water and ethanol and then dried at 80 °C for 2 h. Finally, the as-grown TiO_2 nanorod arrays were annealed at 500 °C for 1 h with a heating rate of 5 °C/min.

2.2. Synthesis of $ZnIn_2S_4$ Nanosheet/TiO_2 Nanorod Arrays. 25 mM of zinc sulfate heptahydrate, 50 mM of indium(III) chloride tetrahydrate, 100 mM of thioacetamide (TAA), and 10 mL of deionized water were added into the autoclave mentioned above and stirred for 20 min. The FTO substrate with the TiO_2 nanorod array was put on the bottom of the Teflon-liner of autoclave. The reaction was performed at 150 °C for 15 min and cooled down to room temperature naturally. Once rinsed with deionized water and ethanol, the sample was dried at 60 °C for 2 h under vacuum.

2.3. Sample Characterizations. The morphology of samples was observed by field-emission scanning electron microscopy (FE-SEM, Hitachi SU8010). The microstructure was analyzed by transmission electron microscopy (TEM) and high-resolution TEM (HRTEM) (FEI Tecnai G2 F20 S-TWIN TMP). The phase was measured by the X-ray diffractometer (XRD). Both the absorption and the reflectance spectra of electrodes were measured by a UV−vis spectrophotometer (Shimadzu UV-3600). For the reflectance measurement, the samples were mounted at the backside of the integrating sphere and the reflectance spectra were normalized to the reflection of a white standard.

2.4. PEC Measurements. PEC properties were obtained by an Autolab electrochemical workstation (PGSTAT 302N). The as-prepared $ZnIn_2S_4/TiO_2$ sample was used as the working electrode and a Pt mesh as the counter electrode, and the reference electrode was a saturated Ag/AgCl electrode. The electrolyte contains 0.35 M Na_2SO_3 and 0.24 M Na_2S (pH 11.5). During the measurement, N_2 was bubbled through to remove the dissolved oxygen in the electrolyte. The photocurrent densities versus measured potential (I−V) and amperometric current−time (I−t) curves with light on/off cycles measurements were performed in a standard three-electrode configuration under AM 1.5G illumination (100 mW/cm^2) provided by a solar light simulator (Newport, 94043A). Electrochemical impedance spectra (EIS) were measured on the same workstation under the open-circuit condition with the frequency range from 0.1 Hz to 100 kHz. Mott−Schottky plots were measured in the dark at an AC frequency of 1.0 kHz.

3. RESULTS AND DISCUSSION

Figure 1 represents typical SEM images and the XRD pattern of the pristine TiO_2 nanorod array films grown on FTO substrates.

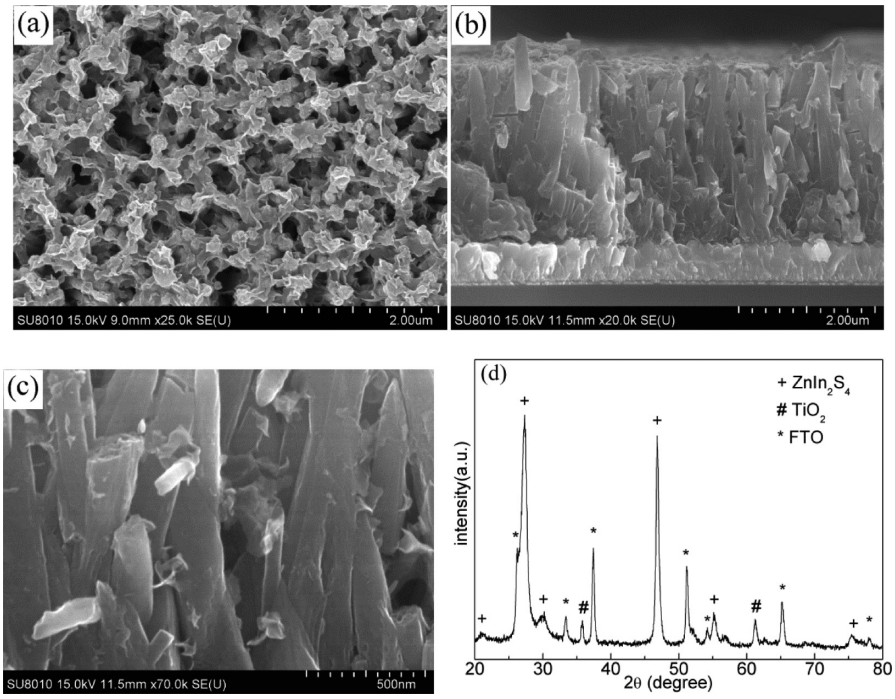

Figure 2. Typical SEM images of $ZnIn_2S_4$ nanosheet/TiO_2 nanorod arrays. (a) Top-view. (b) Cross-sectional view and (c) enlarged image from the central part of (b). (d) XRD pattern.

Figure 1a is a low-magnification image of the nanorod arrays, which shows that the entire surface of the FTO substrate is covered uniformly with TiO_2 nanorods. The higher-magnification image (Figure 1b) indicates that the top facets of the nanorods are square, suggesting the expected growth habit of a tetragonal crystal structure. In addition, the side facets of nanorods are smooth. The cross-sectional view (Figure 1c) of the sample shows that the nanorods are nearly vertical to the FTO substrate and over 2 μm in length, and the diameter of nanorods decreases gradually from bottom to top. The similar phenomenon was also observed previously.[32] To determine the crystal structure, the XRD spectrum was collected from the pristine TiO_2 nanorod array (Figure 1d). After subtracting the diffraction peaks from FTO glass, other diffraction peaks are indexed to the characteristic peaks of tetragonal rutile TiO_2 (JCPDS No. 88-1175), confirming that the as-prepared nanorods are rutile TiO_2.

The surface morphologies of $ZnIn_2S_4$ nanosheet/TiO_2 nanorod arrays are shown in Figure 2a–c. It can be seen that the top surface of the TiO_2 nanorod array is covered by a network of interconnected nanosheets, indicating a high surface area, which have potential applications in the areas of catalysis and energy conversion. The cross-sectional images (Figure 2b,c) demonstrate that the $ZnIn_2S_4$ nanosheets are distributed randomly on the side surface and interstices of nanorods, and the gap between TiO_2 nanorods almost disappears owing to the filling of $ZnIn_2S_4$ nanosheets. Besides the peaks from TiO_2 nanorods and FTO substrate, the diffraction peaks in the XRD pattern (Figure 2d) are attributed to the hexagonal phase of $ZnIn_2S_4$ (JCPDS card No. 65-2023).

Prolonging the growth time of $ZnIn_2S_4$ nanosheets to 30 and 45 min, more nanosheets are deposited and the size of nanosheets becomes larger, forming a layer of a continuous nanosheet film (Figure 3a,b). In addition, the precursor concentration also affects the final morphology of nanostructures. As the concentration is low, only randomly distributed $ZnIn_2S_4$ nuclei are formed because there are not enough species

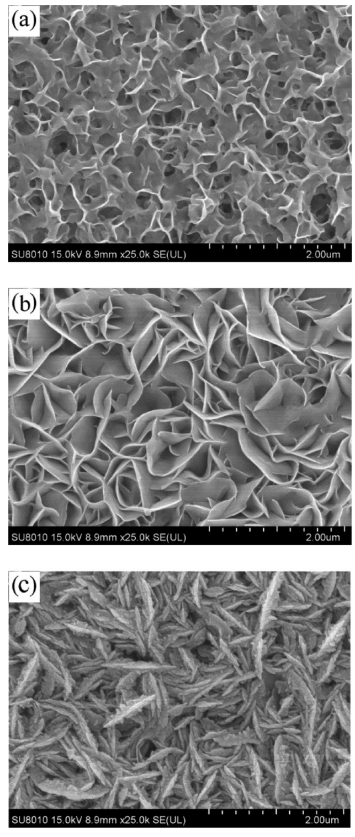

Figure 3. SEM images of $ZnIn_2S_4$ nanosheet/TiO_2 nanorod arrays synthesized at (a) 30 min and (b) 45 min. (c) 45 min at a high precursor concentration.

to make them grow into nanosheets. As the concentration is high, more nucleation centers result in faster growth; thus, nanosheet films are formed rapidly and also the secondary growth occurs. It

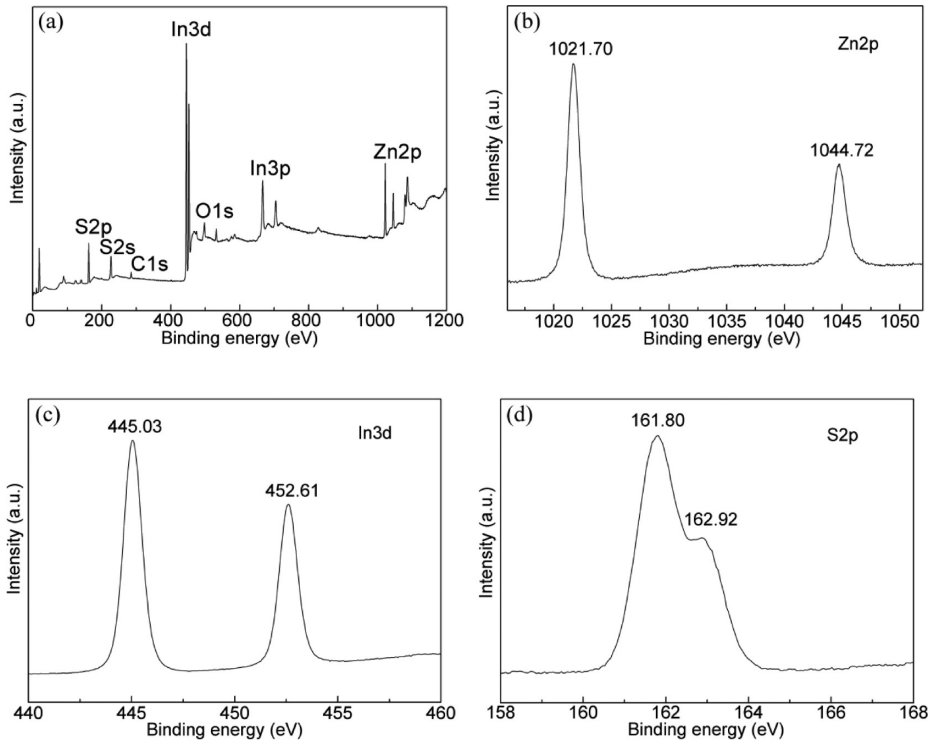

Figure 4. XPS spectrum of as-prepared $ZnIn_2S_4$ nanosheet/TiO_2 nanorod arrays. (a) Survey spectrum. (b–d) High-resolution Zn 2p, In 3d, and S 2p spectra.

can be clearly seen that nanoparticles are grown on the surface of nanosheets when the reaction time is 45 min (Figure 3c). It is worthy to note that it is impossible to obtain $ZnIn_2S_4$ nanosheets directly grown on FTO substrates, because they have very poor adhesion force and would be washed away once rinsing in water. Although the detailed growth mechanism is still not clear, it implies that the TiO_2 nanorod arrays play an important role in the good adherence between $ZnIn_2S_4$ and TiO_2. The hydrothermal reaction processes for the formation of $ZnIn_2S_4$ nanosheets can be described as follows:

$$CH_3CSNH_2 + H_2O \leftrightarrow CH_3CONH_2 + H_2S \quad (1)$$

$$Zn^{2+} + 2In^{3+} + 4H_2S \rightarrow ZnIn_2S_4 + 8H^+ \quad (2)$$

When the TiO_2 nanorod arrays were put into the reaction solution, the Zn^{2+} and In^{3+} can easily diffuse into the gaps between TiO_2 nanorods and are adsorbed on the surface. Once the reaction was carried out at high temperatures, TAA was hydrolyzed to release H_2S, which reacted simultaneously with the Zn^{2+} and In^{3+} to form $ZnIn_2S_4$ nuclei on the TiO_2 nanorod arrays. The final nanosheet morphology was ascribed to an intrinsic lamellar structure of the hexagonal $ZnIn_2S_4$ phase under certain hydrothermal conditions, in which Zn and half of the In atoms are tetrahedrally coordinated by S atoms, whereas the other half are octahedrally coordinated.[33]

To further confirm the composition, the valence states of the $ZnIn_2S_4/TiO_2$ composite are characterized by XPS measurement, as shown in Figure 4. The full scan spectrum indicates the presence of the Zn 2p, In 3d, and S 2p peaks in the sample (Figure 4a) with no obvious impurities detected. The oxygen peak at a binding energy of 532.0 eV originates from H_2O absorbed on the sample surface. The Zn 2p core (Figure 4b) splits into 2p 3/2 (1021.70 eV) and 2p 1/2 (1044.72 eV) peaks, which are consistent with the values for Zn^{2+}. In 3d core shows two peaks at 445.03 eV (3d 5/2) and 452.61 eV (3d 3/2) (Figure 4c), corresponding to In^{3+}. The S 2p 1/2 peak at 161.80 eV is ascribed to S coordinated to Zn and In in $ZnIn_2S_4$ (Figure 4d). All of these results indicate that the chemical states of the sample are Zn^{2+}, In^{3+}, and S^{2-}.[34]

TEM and HRTEM images of the hexagonal $ZnIn_2S_4$ nanosheets are shown in Figure 5. The sample for TEM characterization was obtained by scratching the $ZnIn_2S_4/TiO_2$ film from the FTO glass. It can be seen from Figure 5a that $ZnIn_2S_4$ nanosheets are grown onto the surface of TiO_2 nanorods. The corresponding HRTEM image (Figure 5b)

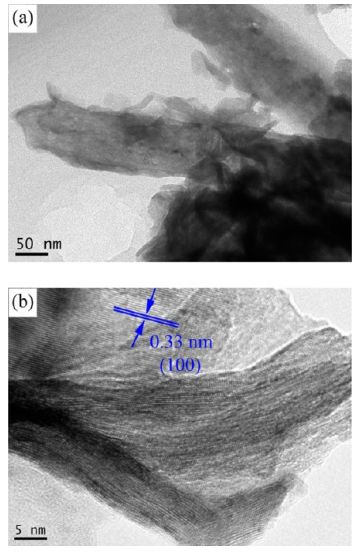

Figure 5. (a) TEM and (b) HRTEM images of 2D $ZnIn_2S_4$ nanosheet/1D TiO_2 nanorod heterojunction.

recorded on the nanosheets exhibits lattice fringes with an interlayer distance of 0.33 nm for the (100) planes of the hexagonal $ZnIn_2S_4$ nanosheet. In the bottom-right corner of this image, we can also find some curved and stacked nanosheets.

The optical properties of the TiO_2 and $ZnIn_2S_4/TiO_2$ were characterized by absorption and reflectance spectra, as shown in Figure 6. We can see that the absorption wavelength of TiO_2

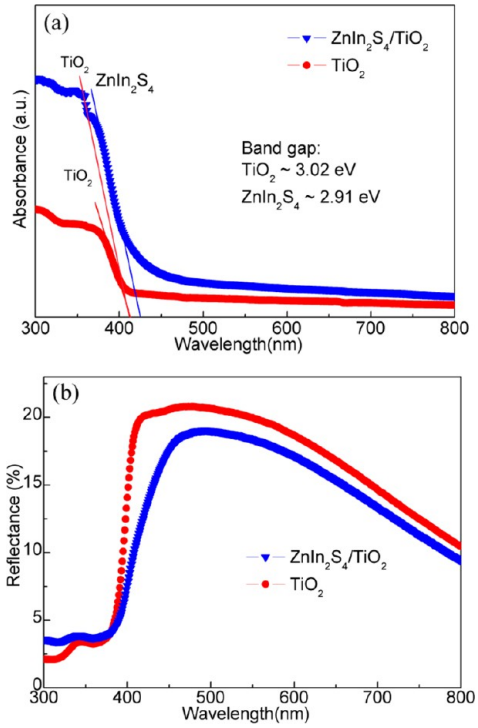

Figure 6. (a) Absorption and (b) reflectance spectra of TiO_2 and $ZnIn_2S_4$ nanosheet/TiO_2 nanorod arrays.

nanorod arrays is less than 410 nm. However, the absorption wavelength of the $ZnIn_2S_4/TiO_2$ is shifted to below 425 nm, suggesting that the combination of $ZnIn_2S_4$ nanosheets for TiO_2 nanorods can expand the absorption range of photoelectrodes (Figure 6a). The relationship between the incident photon energy and the absorption coefficient is given by the following equation: $(\alpha h\nu)^2 = A(h\nu - E_g)$, where α is the optical absorption coefficient, h Planck constant, ν the photon frequency, A a constant, and E_g the band-gap energy of semiconductor. The band-gap values of TiO_2 and $ZnIn_2S_4$ are calculated to be 3.02 and 2.91 eV, respectively. The reflectance spectra (Figure 6b) indicate that the $ZnIn_2S_4/TiO_2$ hybrid structures have lower reflectance than TiO_2 nanorod arrays. This is probably due to the fact that the 1D orientation of TiO_2 nanorod arrays leads to only a single reflection from the nanorod surface. For the hybrid structure, the multiple light scattering happens among the 1D nanorods and 2D polydirectional nanosheets, which increases the light absorption path and interaction sites of nanostructures with incident light. This light trapping effect may contribute to enhanced photocurrent in the process of water splitting.

PEC measurements were performed in a three-electrode cell using a saturated Ag/AgCl as a reference electrode. Hereafter, the electrode potential is converted to the reversible hydrogen electrode (RHE) potential according to the Nernst equation[35]

$$E_{RHE} = E_{Ag/AgCl} + 0.059\text{pH} + E^{o}_{Ag/AgCl}$$

where E_{RHE} is the converted potential versus RHE, $E^{o}_{Ag/AgCl}$ = 0.1976 V at 25 °C, and $E_{Ag/AgCl}$ is the measured potential versus the Ag/AgCl reference. As for the pristine TiO_2 photoelectrode, the onset potential (V_{on}) is about 0.05 V and the maximum photocurrent density is 0.4 mA/cm^2 (Figure 7a). In contrast, the photocurrent density of the $ZnIn_2S_4/TiO_2$ photoelectrode increases from the onset potential around −0.53 V and approaches 1.2 mA/cm^2 at 1.5 V, which shows a 3-fold enhancement at the same applied potential. More importantly, there is no observed saturation of photocurrent density with increasing potential, indicating efficient charge separation in the heterojunction. The enhanced photocurrent density is because electron−hole pairs are separated at the interface of the $ZnIn_2S_4/TiO_2$ heterojunction and then transport along TiO_2 nanorods to the FTO substrate, so that the recombination chance is reduced largely. The significantly negative shift in the onset potential (Fermi energy level) for the $ZnIn_2S_4/TiO_2$ electrode suggests a larger accumulation of electrons in the heterojunction and reflects decreased charge recombination.[36] This analysis is also confirmed by the following Mott−Schottky result.

Figure 7b shows the transient photocurrent curve (I−t) measured at a bias potential of 0.4 V (vs RHE) via several on−off cycles of illumination. Upon illumination, the photocurrent rapidly reaches a steady-state value 0.6 mA/cm^2 and completely reverts to zero once the light is switched off. Such fast rise and fall of the photocurrents indicates that carrier transport in the heterojunction material proceeds very quickly. Furthermore, to investigate the stability of the $ZnIn_2S_4/TiO_2$ photoelectrode, the photocurrent stability measurements were carried out. As shown in Figure 7c, despite that the photocurrent density has large variations in the first 15 min, it possesses a stable value with negligible variations in the following measurement period. To understand the electronic properties of the nanorod arrays in electrolyte solution, we performed electrochemical impedance measurements in the dark to determine the capacitance of electrodes. The carrier density and flat band potential at the nanorod arrays/electrolyte interface can be estimated by the Mott−Schottky (M-S) equation[37]

$$1/C^2 = (2/e_o\varepsilon\varepsilon_o N_d A^2)[(V - V_{FB}) - kT/e_o]$$

where C is the specific capacity, ε is the dielectric constant of $ZnIn_2S_4$ or TiO_2, ε_o is the electric permittivity of vacuum, N_d is the carrier density, A is the area, V is the applied potential, V_{FB} is the flat band potential, k is the Boltzmann constant, T is the absolute temperature, and e_0 is the electron charge. To characterize the photoactivity of the electrodes at various wavelengths, the incident photon-to-current conversion efficiency (IPCE) was measured at 1.1 V (vs RHE) (Figure 7d). The IPCE of the $ZnIn_2S_4/TiO_2$ is higher than that of TiO_2 electrodes across the whole absorption range, indicating that electron−hole pairs are separated more efficiently in the $ZnIn_2S_4/TiO_2$ heterojunction electrodes.

Figure 8a represents the typical M-S curve. By extrapolating the X-intercepts of the linear region in the M-S plot, V_{FB} of TiO_2 and $ZnIn_2S_4/TiO_2$ nanorod arrays is found to be 0.29 and 0.13 V (vs RHE), respectively. Such a negative variation of the flat band potential suggests a higher carrier concentration in the heterojunction and more efficient charge transfer from $ZnIn_2S_4$ to TiO_2 and then to the FTO current collector. In addition, the positive slope indicates that the $ZnIn_2S_4/TiO_2$ nanorod array is an n-type semiconductor with electron conduction. Combing the result of V_{FB} and the band-gap values of semiconductors, the conduction and valence band (CB and VB) positions of TiO_2

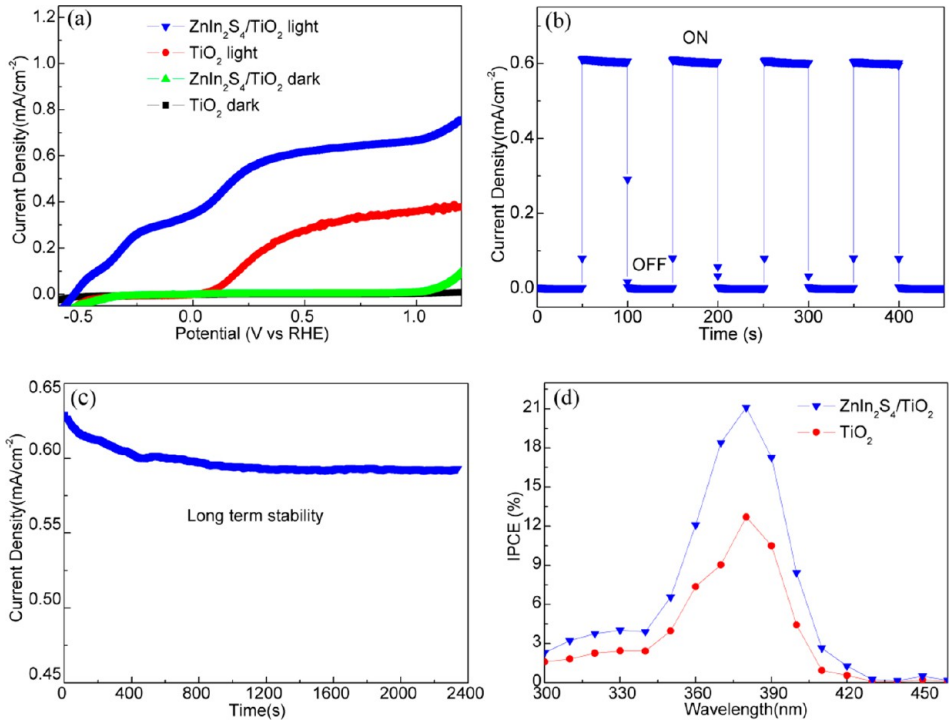

Figure 7. (a) Photocurrent versus applied voltage (I–V) under AM 1.5G in the dark and at 100 mW/cm^2 illumination for pristine TiO_2 and $ZnIn_2S_4$ nanosheet/1D TiO_2 nanorod heterojunction electrodes. (b) Amperometric I–t curve of the $ZnIn_2S_4$ nanosheet/1D TiO_2 nanorod heterojunction electrode at 0.4 V versus RHE with light on/off cycles. (c) Photocurrent stability measurement. (d) IPCE spectra measured at an applied bias of 1.1 V versus RHE.

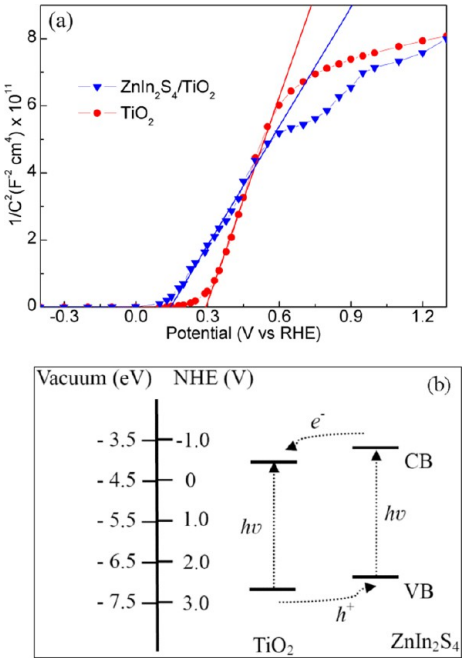

Figure 8. (a) Mott–Schottky plots of pristine TiO_2 and $ZnIn_2S_4$ nanosheet/1D TiO_2 nanorod heterojunction arrays. (b) A schematic mechanism of carrier transferring in $ZnIn_2S_4$ nanosheet/1D TiO_2 nanorod heterojunction system.

and $ZnIn_2S_4$ can be roughly estimated. A possible mechanism of charge transfer in the $ZnIn_2S_4/TiO_2$ hybrid system is proposed in Figure 8b. When the $ZnIn_2S_4/TiO_2$ heterojunction is irradiated by light, electrons are excited to the conduction band of $ZnIn_2S_4$ and TiO_2. Subsequently, electrons migrate from $ZnIn_2S_4$ to TiO_2 and holes are transported in the opposite direction at the heterojunction interface. The separated electrons and holes migrate to the surface as reducing agents to produce H_2 and sacrificial reagents, respectively.

To gain deeper insight into the charge transfer and recombination processes in pristine TiO_2 and $ZnIn_2S_4/TiO_2$ heterojunction electrodes, we compared electrochemical impedance spectra (EIS) measured in the dark (Figure 9a,b) and in light (Figure 9c). On the basis of an equivalent circuit model (the inset in Figure 9a),[38] the transport rate and lifetime of carriers can be derived. Here, R_s is the series resistance, and R_{ct} and C represent the total charge transfer resistance and capacitance of the space charge region, respectively, including charge transfer across the FTO/TiO_2–$ZnIn_2S_4$ interface and the $ZnIn_2S_4$/electrolyte interface. W is the Warburg impedance. R_{Pt} and C_{Pt} are the resistance and capacitance of the Pt cathode. In the dark, the curves are composed of two parts: a minor semicircle at high frequencies corresponding to charge transfer resistance and a major straight line part at low frequencies related to mass transfer resistance. This shows that mass transfer is a dominant process in the dark compared to the charge transfer. In light, an obvious semicircle arc appears at high frequencies and the arc radius for the $ZnIn_2S_4/TiO_2$ heterojunction is much smaller than pristine TiO_2. Normally, the smaller the radius, the lower the charge transfer impedance at the electrode–electrolyte interface.[39] Moreover, the characteristic peak frequency (below 100 Hz) shifts to a lower value for the $ZnIn_2S_4/TiO_2$ heterojunction, as shown in the Bode phase plot in Figure 9d. This means longer electron lifetime than that in the pristine TiO_2 electrode. As we know that the 2D structure also can provide recombination sites for photoexcited charges, thus the lifetime of charges can be decreased. In the present study, to attack this problem of 2D $ZnIn_2S_4$ nanosheets, we designed 2D $ZnIn_2S_4$ nanosheet/1D

dx.doi.org/10.1021/am505015j | ACS Appl. Mater. Interfaces 2014, 6, 17200–17207

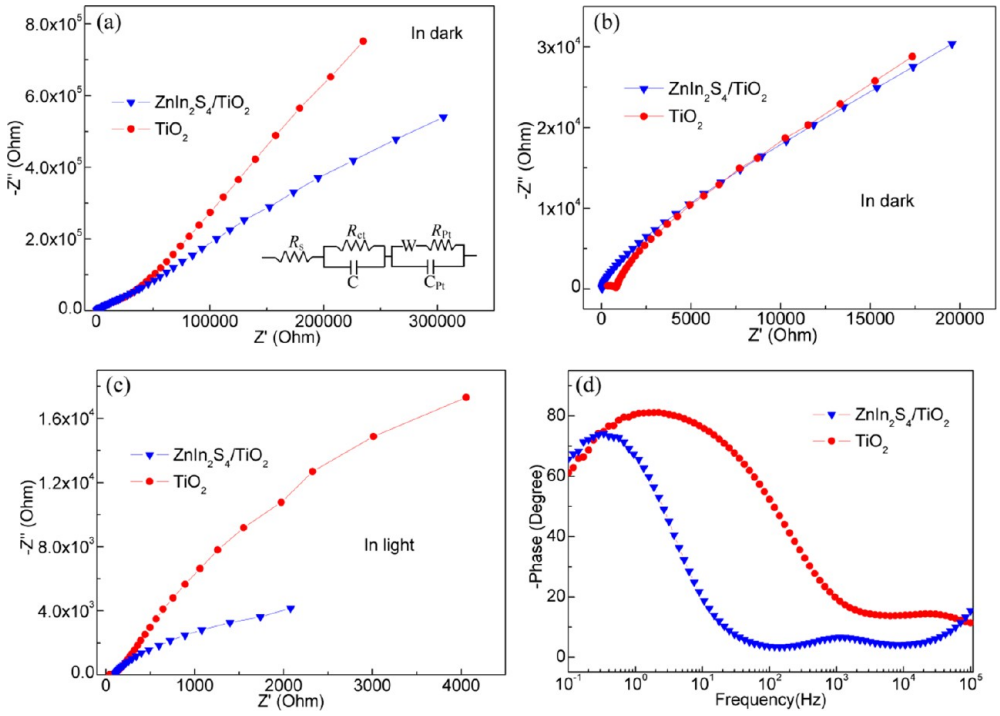

Figure 9. EIS spectra measured at an open-circuit voltage. (a–c) Nyquist plots under dark and light illumination. An equivalent circuit model is inserted in (a). (d) Bode phase plots.

TiO_2 nanorod array heterojunctions, which can increase the lifetime of charges mainly benefiting from two factors to: (1) Heterojunctions effectively separate photoexcited electrons and holes, and the 1D pathway of TiO_2 nanorods can rapidly transport separated electrons coming from $ZnIn_2S_4$ nanosheets to collection electrodes for producing hydrogen, ultimately minimizing the chance of recombination losses occurring in $ZnIn_2S_4$ nanosheets. (2) The amount of deposited 2D $ZnIn_2S_4$ nanosheets should not be high; otherwise, the transport distance of charges in nanosheets is very long and thus increases the recombination. This point can be confirmed by *I*–*V* results, as shown in Figure 10. It can be seen that photocurrent decreases with increasing the growth time of $ZnIn_2S_4$ nanosheets (SEM images are shown in Figure 3a,b). From these analyses, the present heterojunction provides several advantages of more effective electron–hole separation, faster interface charge transfer, and longer electron lifetime, thus resulting in improved PEC performance.

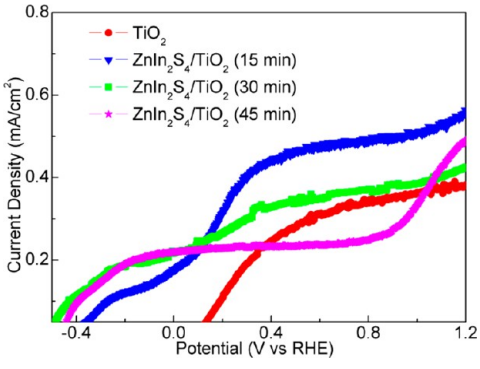

Figure 10. *I*–*V* curves of $ZnIn_2S_4$ nanosheet/1D TiO_2 nanorod heterojunction arrays synthesized at different times (15, 30, and 45 min).

4. CONCLUSION

In summary, we have designed and developed novel 2D $ZnIn_2S_4$ nanosheet/1D TiO_2 nanorod heterojunction arrays as photoelectrodes for PEC water splitting. Because of this heterojunction structure, its photoelectrode demonstrates enhanced photocurrent density (1.2 mA/cm^2, AM 1.5G), which is 3 times higher than that of pristine TiO_2, and the onset potential is largely shifted to −0.53 V from 0.05 V. The fast electron–hole separation, excellent charge transfer, and enhanced carrier lifetime contribute to the enhanced PEC properties. We hope that our findings open a promising route to design complex 2D/1D nanostructures and apply them in solar cells and other nanodevices.

AUTHOR INFORMATION

Corresponding Author

*E-mail: lli@suda.edu.cn, liang.li0216@gmail.com (L.L.).

Notes

The authors declare no competing financial interest.

ACKNOWLEDGMENTS

We acknowledge the support from the National Natural Science Foundation (51422206, 51372159, 11304217), 1000 Youth Talents Plan, Jiangsu Shuangchuang Plan, a Project Supported by Jiangsu Scientific and Technology Committee for Distinguished Young Scholars (BK20140009) and Funded by the Priority Academic Program Development of Jiangsu Higher Education Institutions (PAPD).

REFERENCES

(1) Fujishima, A.; Honda, K. Electrochemical Photolysis of Water at a Semiconductor Electrode. *Nature* **1972**, *238*, 37–38.

(2) Chen, X.; Shen, S.; Guo, L.; Mao, S. S. Semiconductor-Based Photocatalytic Hydrogen Generation. *Chem. Rev.* **2010**, *110*, 6503–6570.

(3) Walter, M. G.; Warren, E. L.; McKone, J. R.; Boettcher, S. W.; Mi, Q.; Santori, E. A.; Lewis, N. S. Solar Water Splitting Cells. *Chem. Rev.* **2010**, *110*, 6446−6473.
(4) Nozik, A. J. Photoelectrolysis of Water Using Semiconducting TiO_2 Crystals. *Nature* **1975**, *257*, 383−386.
(5) Hoang, S.; Guo, S.; Hahn, N. T.; Bard, A. J.; Mullins, C. B. Visible Light Driven Photoelectrochemical Water Oxidation on Nitrogen-Modified TiO_2 Nanowires. *Nano Lett.* **2012**, *12*, 26−32.
(6) Cho, I. S.; Logar, M.; Lee, C. H.; Cai, L.; Prinz, F. B.; Zheng, X. Rapid and Controllable Flame Reduction of TiO_2 Nanowires for Enhanced Solar Water-Splitting. *Nano Lett.* **2014**, *14*, 24−31.
(7) Bian, J.; Huang, C.; Wang, L.; Hung, T.; Daoud, W. A.; Zhang, R. Carbon Dot Loading and TiO_2 Nanorod Length Dependence of Photoelectrochemical Properties in Carbon Dot/TiO_2 Nanorod Array Nanocomposites. *ACS Appl. Mater. Interfaces* **2014**, *6*, 4883−4890.
(8) Linsebigler, A. L.; Lu, G.; Yates, J. T. Photocatalysis on TiO_2 Surfaces: Principles, Mechanisms, and Selected Results. *Chem. Rev.* **1995**, *95*, 735−758.
(9) Hwang, Y. J.; Hahn, C.; Liu, B.; Yang, P. Photoelectrochemical Properties of TiO_2 Nanowire Arrays: A Study of the Dependence on Length and Atomic Layer Deposition Coating. *ACS Nano* **2012**, *6*, 5060−5069.
(10) Emeline, A. V.; Furubayashi, Y.; Zhang, X.; Jin, M.; Murakami, T.; Fujishima, A. Photoelectrochemical Behavior of Nb-Doped TiO_2 Electrodes. *J. Phys. Chem. B* **2005**, *109*, 24441−24444.
(11) Luo, S. Y.; Yan, B. X.; Shen, J. Intense Photocurrent from Mo-Doped TiO_2 Film with Depletion Layer Array. *ACS Appl. Mater. Interfaces* **2014**, *6*, 8942−8946.
(12) Liu, N.; Schneider, C.; Freitag, D.; Hartmann, M.; Venkatesan, U.; Müller, J.; Spiecker, E.; Schmuki, P. Black TiO_2 Nanotubes: Cocatalyst-Free Open-Circuit Hydrogen Generation. *Nano Lett.* **2014**, *14*, 3309−3313.
(13) Pu, Y. C.; Ling, Y.; Chang, K. D.; Liu, C. M.; Zhang, J. Z.; Hsu, Y. J.; Li, Y. Surface Passivation of TiO_2 Nanowires Using a Facile Precursor-Treatment Approach for Photoelectrochemical Water Oxidation. *J. Phys. Chem. C* **2014**, *118*, 15086−15094.
(14) Cho, I. S.; Chen, Z.; Forman, A. J.; Kim, D. R.; Rao, P. M.; Jaramillo, T. F.; Zheng, X. Branched TiO_2 Nanorods for Photoelectrochemical Hydrogen Production. *Nano Lett.* **2011**, *11*, 4978−4984.
(15) Zhang, Z. H.; Wang, P. Optimization of Photoelectrochemical Water Splitting Performance on Hierarchical TiO_2 Nanotube Arrays. *Energy Environ. Sci.* **2012**, *5*, 6506−6512.
(16) Kim, H.; Yong, K. A Highly Efficient Light Capturing 2D (nanosheet)−1D (nanorod) Combined Hierarchical ZnO Nanostructure for Efficient Quantum Dot Sensitized Solar Cells. *Phys. Chem. Chem. Phys.* **2013**, *15*, 2109−2116.
(17) Pan, K.; Dong, Y.; Zhou, W.; Pan, Q.; Xie, Y.; Xie, T.; Tian, G.; Wang, G. Facile Fabrication of Hierarchical TiO_2 Nanobelt/ZnO Nanorod Heterogeneous Nanostructure: An Efficient Photoanode for Water Splitting. *ACS Appl. Mater. Interfaces* **2013**, *5*, 8314−8320.
(18) Luo, J.; Ma, L.; He, T.; Ng, C. F.; Wang, S.; Sun, H.; Fan, H. J. TiO_2/(CdS, CdSe, CdSeS) Nanorod Heterostructures and Photoelectrochemical Properties. *J. Phys. Chem. C* **2012**, *116*, 11956−11963.
(19) Li, J.; Cushing, S. K.; Zheng, P.; Senty, T.; Meng, F.; Bristow, A. D.; Manivannan, A.; Wu, N. Solar Hydrogen Generation by a CdS-Au-TiO_2 Sandwich Nanorod Array Enhanced with Au Nanoparticle as Electron Relay and Plasmonic Photosensitizer. *J. Am. Chem. Soc.* **2014**, *136*, 8438−8449.
(20) Lu, M.; Shao, C.; Wang, K.; Lu, N.; Zhang, X.; Zhang, P.; Zhang, M.; Li, X.; Liu, Y. *p*-MoO_3 Nanostructures/*n*-TiO_2 Nanofiber Heterojunctions: Controlled Fabrication and Enhanced Photocatalytic Properties. *ACS Appl. Mater. Interfaces* **2014**, *6*, 9004−9012.
(21) Seo, W. S.; Otsuka, R.; Okuno, H.; Ohta, M.; Koumoto, K. Thermoelectric Properties of Sintered Polycrystalline $ZnIn_2S_4$. *J. Mater. Res.* **1999**, *14*, 4176−4181.
(22) Romeo, N.; Dallaturca, A.; Braglia, R.; Sberveglieri, G. Charge Storage in $ZnIn_2S_4$ Single Crystals. *Appl. Phys. Lett.* **1973**, *22*, 21−22.
(23) Lei, Z.; You, W.; Liu, M.; Zhou, G.; Takata, T.; Hara, M.; Domen, K.; Li, C. Photocatalytic Water Reduction under Visible Light on a Novel $ZnIn_2S_4$ Catalyst Synthesized by Hydrothermal Method. *Chem. Commun.* **2003**, 2142−2143.
(24) Xu, B.; He, P.; Liu, H.; Wang, P.; Zhou, G.; Wang, X. A 1D/2D Helical CdS/$ZnIn_2S_4$ Nano-Heterostructure. *Angew. Chem., Int. Ed.* **2014**, *53*, 1−6.
(25) Shen, S.; Zhao, L.; Zhou, Z.; Guo, L. Enhanced Photocatalytic Hydrogen Evolution over Cu-Doped $ZnIn_2S_4$ under Visible Light Irradiation. *J. Phys. Chem. C* **2008**, *112*, 16148−16155.
(26) Shen, S.; Chen, X.; Ren, F.; Kronawitter, C. X.; Mao, S. S.; Guo, L. Solar Light-Driven Photocatalytic Hydrogen Evolution over $ZnIn_2S_4$ Loaded with Transition-Metal Sulfides. *Nanoscale Res. Lett.* **2011**, *6*, 290−295.
(27) Zhou, M.; Lou, X. W.; Xie, Y. Two-Dimensional Nanosheets for Photoelectrochemical Water Splitting: Possibilities and Opportunities. *Nano Today* **2013**, *8*, 598−618.
(28) Li, C.; Yu, Y.; Chi, M.; Cao, L. Epitaxial Nanosheet−Nanowire Heterostructures. *Nano Lett.* **2013**, *13*, 948−953.
(29) Liu, J.; Jiang, J.; Cheng, C.; Li, H.; Zhang, J.; Gong, H.; Fan, H. J. Co_3O_4 Nanowire@MnO_2 Ultrathin Nanosheet Core-Shell Arrays: A New Class of High-Performance Pseudocapacitive Materials. *Adv. Mater.* **2011**, *23*, 2076−2081.
(30) Zhang, G.; Fang, H.; Yang, H.; Jauregui, L. A.; Chen, Y. P.; Wu, Y. Design Principle of Telluride-Based Nanowire Heterostructures for Potential Thermoelectric Applications. *Nano Lett.* **2012**, *12*, 3627−3633.
(31) Zhou, W.; Cao, X.; Zeng, Z.; Shi, W.; Zhu, Y.; Yan, Q.; Liu, H.; Wang, J.; Zhang, H. One-step Synthesis of Ni_3S_2 Nanorod@$Ni(OH)_2$ Nanosheet Core−Shell Nanostructures on a Three-Dimensional Graphene Network for High-Performance Supercapacitors. *Energy Environ. Sci.* **2013**, *6*, 2216−2221.
(32) Wang, H.; Bai, Y.; Wu, Q.; Zhou, W.; Zhang, H.; Li, J.; Guo, L. Rutile TiO_2 Nano-Branched Arrays on FTO for Dye-Sensitized Solar Cells. *Phys. Chem. Chem. Phys.* **2011**, *13*, 7008−7013.
(33) Gou, X. L.; Cheng, F. Y.; Shi, Y. H.; Zhang, L.; Peng, S. J.; Chen, J.; Shen, P. W. Shape-Controlled Synthesis of Ternary Chalcogenide $ZnIn_2S_4$ and $CuIn(S,Se)_2$ Nano-/Microstructures *via* Facile Solution Route. *J. Am. Chem. Soc.* **2006**, *128*, 7222−7229.
(34) Peng, S.; Zhu, P.; Thavasi, V.; Mhaisalkara, S. G.; Ramakrishna, S. Facile Solution Deposition of $ZnIn_2S_4$ Nanosheet Films on FTO Substrates for Photoelectric Application. *Nanoscale* **2011**, *3*, 2602−2608.
(35) Grätzel, M. Photoelectrochemical Cells. *Nature* **2001**, *414*, 338−344.
(36) Hou, Y.; Zuo, F.; Dagg, A.; Feng, P. Visible Light-Driven α-Fe_2O_3 Nanorod/Graphene/$BiV_{1-x}Mo_xO_4$ Core/Shell Heterojunction Array for Efficient Photoelectrochemical Water Splitting. *Nano Lett.* **2012**, *12*, 6464−6473.
(37) Wolcott, A.; Smith, W. A.; Kuykendall, T. R.; Zhao, Y.; Zhang, J. Z. Photoelectrochemical Water Splitting Using Dense and Aligned TiO_2 Nanorod Arrays. *Small* **2009**, *5*, 104−111.
(38) Li, H.; Cheng, C.; Li, X.; Liu, J.; Guan, C.; Tay, Y. Y.; Fan, H. J. Composition-Graded $Zn_xCd_{1-x}Se$@ZnO Core−Shell Nanowire Array Electrodes for Photoelectrochemical Hydrogen Generation. *J. Phys. Chem. C* **2012**, *116*, 3802−3807.
(39) Hou, Y.; Zuo, F.; Dagg, A.; Feng, P. A Three-Dimensional Branched Cobalt-Doped α-Fe_2O_3 Nanorod/$MgFe_2O_4$ Heterojunction Array as a Flexible Photoanode for Efficient Photoelectrochemical Water Oxidation. *Angew. Chem., Int. Ed.* **2013**, *52*, 1248−1252.